CERN – EUROPEAN ORGANIZATION FOR NUCLEAR RESEARCH

CLIC – Note – 1138

INTEGRATED SIMULATION OF DYNAMIC EFFECTS FOR THE 380 GEV CLIC DESIGN

Chetan Gohil[1], Daniel Schulte[2], Philip N. Burrows[1]

[1]JAI, University of Oxford, Oxford, United Kingdom
[2]CERN, Geneva, Switzerland

CERN-ACC-2018-0051
14/11/2018

Abstract

Integrated simulations of the Ring to Main Linac, Main Linac and Beam Delivery System of the 380 GeV CLIC design are presented. The performance of a perfect lattice and the effect of dynamic imperfections are studied. The dynamic effects investigated were ground motion, stray magnetic fields and longitudinal stability. The effectiveness of different mitigation methods for ground motion and stray magnetic fields was also studied.

Geneva, Switzerland
14 November 2018

Integrated Simulation of Dynamic Effects for the 380 GeV CLIC Design

C. Gohil[1], D. Schulte[2], and P.N. Burrows[1]

[1]JAI, University of Oxford, Oxford, OX1 3PA, United Kingdom
[2]CERN, Geneva, Switzerland

(November 14, 2018)

Abstract

Integrated simulations of the Ring to Main Linac, Main Linac and Beam Delivery System of the 380 GeV CLIC design are presented. The performance of a perfect lattice and the effect of dynamic imperfections are studied. The dynamic effects investigated were ground motion, stray magnetic fields and longitudinal stability. The effectiveness of different mitigation methods for ground motion and stray magnetic fields was also studied.

1 Integrated Simulations

A simulation of the 380 GeV CLIC design starting from the exit of the Damping Rings (DRs) to the Interaction Point (IP) was developed. The Ring to Main Linac (RTML), Main Linac (ML) and Beam Delivery System (BDS) were integrated into a single simulation. Two different BDS designs that differ in the drift length (L^*) from the final quadrupole to the IP were studied.

Both the electron and positron beams were simulated independently. Although, the RTML beamline for the positron beam differs from the electron RTML beamline, the electron RTML beamline was used in the simulation of the positron beam, such that both the electron and positron beamlines are mirrored.

Simulations were performed with the particle tracking code PLACET [1] and luminosity was calculated with GUINEA-PIG [2].

2 Ideal and Nominal Performance

The preservation of emittance is a key challenge required to meet the designed performance of CLIC. The allocated budgets of emittance growth in each section due to static and dynamic effects are presented in Tab. 1. In this paper only the dynamic budget is of concern.

The perfect lattice, absent of mis-alignments or any other imperfections, was simulated 500 times with different seeds used to generate the initial particle distribution. The luminosity that can be achieved with a perfect lattice is

$$\mathcal{L}_0 = \begin{cases} (4.25 \pm 0.09) \times 10^{34}\ \mathrm{cm^{-2}s^{-1}} & \text{for } L^* = 4.3\ \mathrm{m}, \\ (4.3 \pm 0.1) \times 10^{34}\ \mathrm{cm^{-2}s^{-1}} & \text{for } L^* = 6\ \mathrm{m}. \end{cases} \quad (1)$$

Section	ϵ_x (nm)	ϵ_y (nm)	$\Delta\epsilon_x$ (nm)			$\Delta\epsilon_y$ (nm)		
			Design	Static	Dynamic	Design	Static	Dynamic
RTML	850	10	100	20	30	1	2	2
ML	900	20	15	15	20	0.1	1	8.9
BDS	950	30	0	15	15	0	5	5

Table 1: Targeted final horizontal and vertical normalised emittance (ϵ_x and ϵ_y respectively) and horizontal and vertical normalised emittance growth budgets ($\Delta\epsilon_x$ and $\Delta\epsilon_y$ respectively) of each section due to the design and for static and dynamic imperfections.

	ϵ_x (nm)	ϵ_y (nm)	σ_x (μm)	σ_y (μm)	σ_z (μm)	E (GeV)	δ_E (%)
DR	700	5.00	15.8	0.67	1800	2.86	0.11
RTML	762	5.57	18.7	0.61	68	8.99	0.95
ML	775	5.64	7.90	0.28	68	190	0.34
BDS ($L^* = 4.3$ m)	750	6.28	0.127	0.0013	68	190	0.34
BDS ($L^* = 6$ m)	785	6.28	0.130	0.0013	68	190	0.34

Table 2: Electron beam parameters calculated with PLACET at the end of each section using the perfect lattice, where ϵ_x (ϵ_y) is the horizontal (vertical) emittance, σ_x (σ_y) is the horizontal (vertical) beam size, σ_z is the bunch length, E is the energy and δ_E is the energy spread of the beam.

A large number of macro-particles (100,000) was tracked to ensure that the error on the luminosity remains with a few percent.

The beam parameters at the end of each section of the perfect lattice are shown in Tab. 2. It is clear from Tab. 2 that the integrated simulations perform comfortably within the emittance growth budget allocated for the design.

The luminosity with a vertical offset between colliding beams (beam-beam offset) may be written as

$$\mathcal{L} = \mathcal{L}_0 \exp\left(-\frac{\Delta y^2}{4\sigma_y^2}\right), \tag{2}$$

where $\mathcal{L}_0$ is the ideal luminosity, Δy is the beam-beam offset, σ_y is the vertical beam size and the hourglass effect has been ignored. However, this behaviour is strongly influenced by the electromagnetic interaction of the colliding beams (beam-beam effects). Fig. 1(a) shows a beam-beam offset scan calculated with GUINEA-PIG of a beam tracked through the perfect lattice. Fig. 1(a) shows that the luminosity falls quicker than what is expected from Eq. (2), suggesting that the smaller beam size in the ideal case is resulting in a larger disruption due to beam-beam effects of the two beams at the IP.

To examine the performance under nominal conditions, the emittance from the DRs was increased to provide a horizontal emittance of 920 nm and vertical emittance of 20 nm at the start of the BDS. In this simulation the luminosity obtained was

$$\mathcal{L}_0 = \begin{cases} (2.03 \pm 0.01) \times 10^{34}\ \text{cm}^{-2}\text{s}^{-1} & \text{for } L^* = 4.3\ \text{m}, \\ (2.01 \pm 0.01) \times 10^{34}\ \text{cm}^{-2}\text{s}^{-1} & \text{for } L^* = 6\ \text{m}. \end{cases} \tag{3}$$

Fig. 1(b) shows a beam-beam offset scan under nominal conditions. Here, the behaviour is closer to Eq. (2). It is clear from Fig. 1 that a small offset would lead to a larger luminosity loss in the ideal case compared to the nominal case.

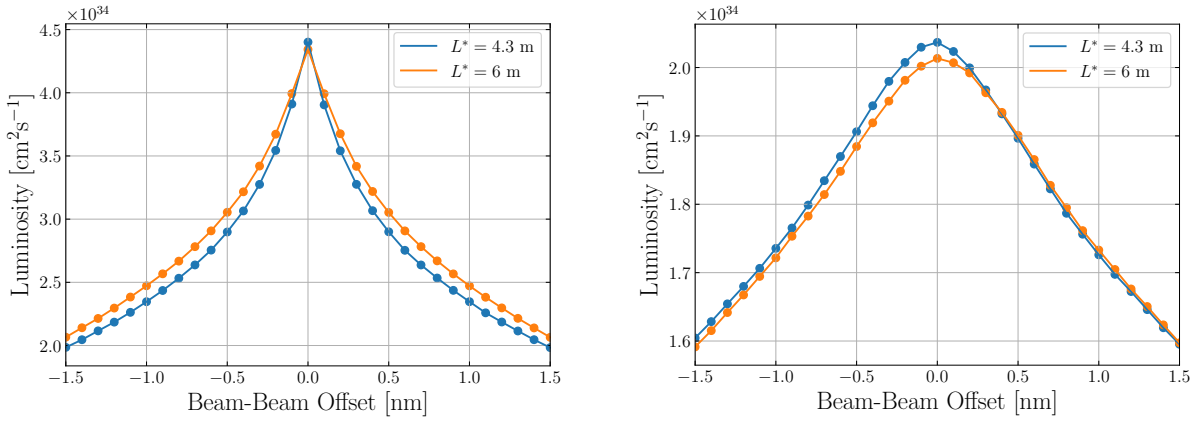

(a) Ideal.

(b) Nominal.

Figure 1: Beam-beam offset scans calculated with beams tracked through a perfect lattice.

3 Ground Motion

Luminosity is reduced due to ground motion in two ways: a beam-beam offset at the IP due to the displacement of magnets close to the IP and an emittance growth along the beamline due to offsets of RTML and ML quadrupoles. Ground motion can be divided into two regimes: one for low frequencies, which impacts on emittance preservation and one for high frequencies, which impacts on the beam-beam offset. The budget for luminosity loss due to ground motion is 3 %.

There are two types of models that are commonly used in ground motion simulations: short-term models valid for time scales up to one minute, which involve power spectral densities (PSDs) and a long-term model valid for time scales of hours, known as the ATL-law. Only the effect of short-term PSD models of ground motion are studied here. The severity of ground motion depends on the site at which the accelerator is placed. Measurements have been performed at several sites and used to fit models to characterise the PSD of ground motion. Four measurements at different sites have been used to develop the models shown in Fig. 2. Model A is based on a measurement in an empty LEP tunnel, this was a very quiet site. Model B is based on measurements on the Fermilab site. Model B10 is a modified version of model B, where additional peaks to match measurements from LAPP (Annecy) and technical noise in the CMS hall are included. Model C is based on measurements at HERA, which is a urbanised location containing high levels of cultural noise. This is considered to be a very noisy site that does not represent the environment that CLIC would be built on.

To prevent luminosity loss due to ground motion, a number of mitigation techniques have been investigated. These include a beam-based feedback system, which corrects the trajectory of the beam as it traverses the accelerator. The effect of the current design of the beam-based feedback system for CLIC is given by the transfer function shown in Fig. 3. This transfer function acts directly on the PSD model used to generate the displacement of elements in the simulations of ground motion. However, this is a simplification as the beam-based feedback does not act directly on the ground motion, but its effect is equivalently modelled as a reduced PSD. As shown in Fig. 3, the beam-based feedback system is not effective for frequencies greater than 1 Hz. For higher frequencies two types of mechanical stabilisation systems are used. The quadrupoles in the accelerator will be

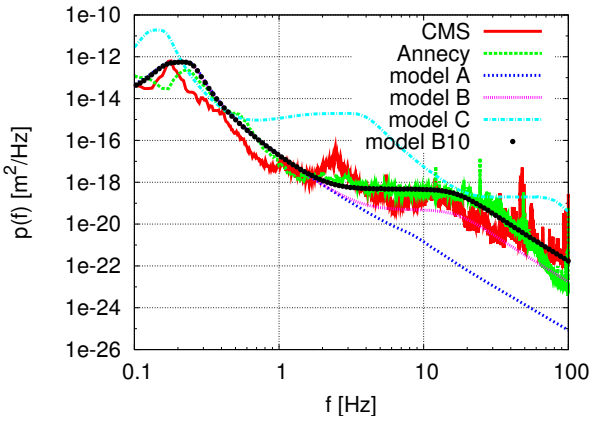

Figure 2: Ground motion PSDs for several sites.

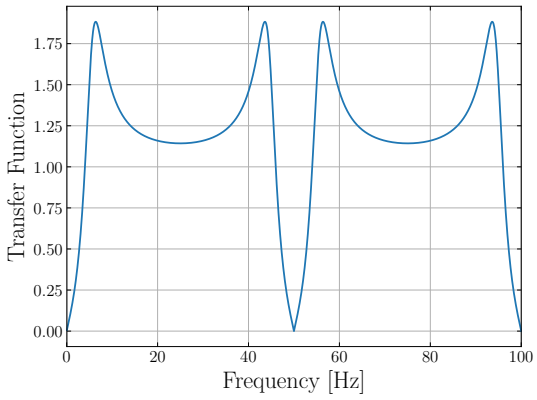

Figure 3: Transfer function of the beam-based feedback system.

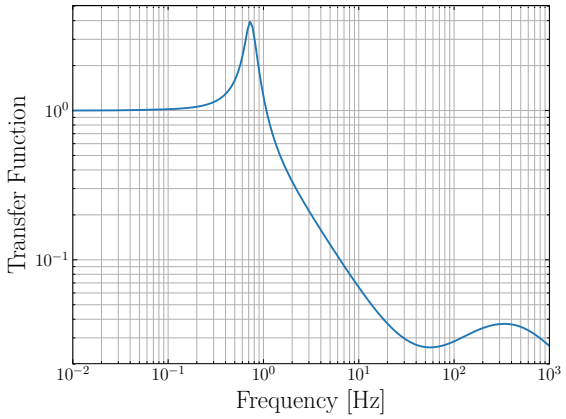

(a) Quadrupole stabilisation system.

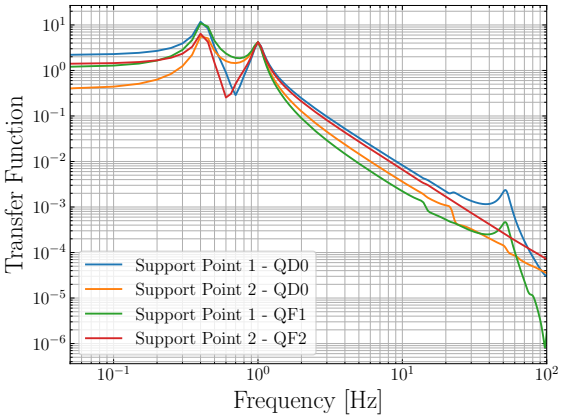

(b) Preisolator.

Figure 4: Transfer functions of the mechanical stabilisation systems considered.

placed on an active stabilisation system, referred to as the quadrupole stabilisation system. This system acts to directly reduce ground motion with the transfer function shown in Fig. 4(a). Another mechanical stabilisation is considered solely for the final doublet in the BDS, where the last two quadrupoles (QD0 and QF1) are placed onto a large mass, referred to as the preisolator. The effect of the mechanical stabilisation systems is to directly reduce the PSD of ground motion. The preisolator is supported at two points, each with their own transfer functions, shown in Fig. 4(b), which are implemented in the integrated simulations.

The RTML contains a turn-around loop. However, the model for ground motion used describes the horizontal and vertical element displacement as a function of distance along the machine. In the integrated simulations, the RTML was 'unfolded' as if the accelerator was one long straight line. This simplification has little effect on the performance loss due to ground motion because virtually all of the effect occurs in the ML and BDS. Tab. 3 shows the luminosity loss with ground motion acting only on one section of CLIC.

The luminosity loss due to different ground motion models acting on a perfect lattice is shown in Tab. 4. 500 pulses spaced 20 ms apart were simulated and their luminosities were averaged. Therefore, the time period over which ground motion was simulated was 10 s. The luminosity recovery of different mitigation techniques is also shown in Tab. 4.

	$L^* = 4.3$ m	$L^* = 6$ m
RTML	0.17	0.33
ML	32	18
BDS	67	63

Table 3: Luminosity loss as a percentage of the perfect lattice luminosity shown in Eq. (1) with ground motion model B10 applied to one section only. No mitigation was applied.

		A	**B**	**B10**	**C**
$L^* = 4.3$ m					
	No Mitigation	47	44	68	90
	Beam-Based Feedback	2.3	62	74	93
	Quadrupole Stabilisation	48	54	54	88
	Preisolator	66	59	62	90
	Quadrupole Stabilisation + Preisolator	66	57	57	85
	Beam-Based Feedback + Preisolator	8.9	26	47	85
	Beam-Based Feedback + Quadrupole Stabilisation	2.0	4.6	15	66
	Beam-Based Feedback + Quadrupole Stabilisation + Preisolator	7.2	5.5	9.3	53
$L^* = 6$ m					
	No Mitigation	55	68	64	91
	Beam-Based Feedback	12	56	71	97
	Quadrupole Stabilisation	56	70	70	93
	Preisolator	66	63	58	93
	Quadrupole Stabilisation + Preisolator	65	67	67	86
	Beam-Based Feedback + Preisolator	8.6	24	45	95
	Beam-Based Feedback + Quadrupole Stabilisation	6.3	8.8	18	72
	Beam-Based Feedback + Quadrupole Stabilisation + Preisolator	9.0	6.9	8.8	54

Table 4: Luminosity loss due to different ground motion models expressed as a percentage of the perfect lattice luminosity given in Eq. (1).

		A	**B**	**B10**	**C**
$L^* = 4.3$ m					
	No Mitigation	22	17	47	83
	Beam-Based Feedback	0.16	34	56	87
	Quadrupole Stabilisation	22	25	25	79
	Preisolator	45		35	79
	Quadrupole Stabilisation + Preisolator	45	31	31	85
	Beam-Based Feedback + Preisolator	45	31	18	88
	Beam-Based Feedback + Quadrupole Stabilisation	0.10	0.37	2.2	42
	Beam-Based Feedback + Quadrupole Stabilisation + Preisolator	0.56	0.49	1.0	25
$L^* = 6$ m					
	No Mitigation	41	50	42	83
	Beam-Based Feedback	0.86	29	52	94
	Quadrupole Stabilisation	42	56	56	85
	Preisolator	42	36	32	80
	Quadrupole Stabilisation + Preisolator	42	40	40	84
	Beam-Based Feedback + Preisolator	42	40	18	82
	Beam-Based Feedback + Quadrupole Stabilisation	0.22	0.70	3.2	53
	Beam-Based Feedback + Quadrupole Stabilisation + Preisolator	0.48	0.43	0.79	29

Table 5: Luminosity loss due to different ground motion models expressed as a percentage of the luminosity given in Eq. (3). Simulations were performed with the emittance from the DRs increased such that the beam enters the BDS with a horizontal emittance of 920 nm and vertical emittance of 20 nm.

The luminosity loss due to the different ground motion models with nominal emittance at the start of the BDS is shown in Tab. 5. The luminosity recovery of different mitigation techniques are also shown in Tab. 5. It is clear from these simulations that model A has the least impact on performance, with just the beam-based feedback being enough to recovery luminosity to within the 3 % luminosity loss budget for ground motion. Luminosity can be recovered to within the budget with just the beam-based feedback and quadrupole stabilisation for model B10, with a further benefit being provided by the preisolator. Model B10 represents a level of ground motion above which CLIC is expected to operate in, i.e. is a pessimistic model. The fact that the luminosity loss can be kept within the budget with mitigation for model B10 ensures that ground motion will not pose a problem for CLIC. Model C represents an environment in which CLIC cannot operate.

		Ideal	Nominal
$L^* = 4.3$ m			
	Direct Effect	38	11
	Beam Pipe	38	9
	Beam-Based Feedback	14	1.4
	Beam Pipe + Beam-Based Feedback	14	1.3
$L^* = 6$ m			
	Direct Effect	48	20
	Beam Pipe	48	17
	Beam-Based Feedback	20	2.9
	Beam Pipe + Beam-Based Feedback	20	2.7

Table 6: Luminosity loss due to a geomagnetic disturbance expressed as a percentage of the perfect lattice luminosity given in Eq. (1) for the ideal case and Eq. (3) for the nominal case.

4 Stray Magnetic Fields

Another source of luminosity loss studied was external (referred to as stray) magnetic fields, of which only dynamic stray fields pose a problem. This is due to static fields being removed by tuning. Stray magnetic fields kick the beam directly and lead to luminosity loss either by inducing a beam-beam offset or by causing emittance growth as the beam traverses the accelerator. Multiple studies of sinusoidal stray magnetic fields has shown nT tolerances to remain within a 2 % luminosity loss budget [3, 4, 5, 6]. Tolerances down to 0.1 nT for particular spatial wavelengths and tolerances of 1 nT for coherent (constant value, symmetric about the IP) stray fields have been reported in [6] for the 380 GeV CLIC design.

There is an on-going campaign to measure and characterise the PSD of stray magnetic fields so that it may be used to study their effect on performance in integrated simulations. No two-dimensional (temporal and spatial) models, such as models A, B, B10, C for ground motion, exist for stray fields. However, there are one-dimensional (temporal) models that represent coherent stray fields. Such stray fields arise from natural sources and are described in [7]. The effect on performance of a geomagnetic disturbance, which represents a worst case scenario of stray fields from natural sources, is studied in this paper.

Fig. 5 shows the PSD of a geomagnetic disturbance measured in Tihany, Hungary (courtesy of B. Heilig) used as the model in integrated simulations for stray fields. The luminosity loss due to model is shown in Tab. 6. The effect of the beam pipe and beam-based feedback system is also shown in Tab. 6. The CLIC beam pipe was modelled as a cylinder of inner radius 1 cm, consisting of 20 μm of copper and 1 mm of steel. The beam pipe acts to attenuate some of the stray field with the transfer function shown in Fig. 6(a). It can be seen from Fig. 6(a) that the beam pipe has little effect on the stray field. However, shown in Fig. 6(b) is the attenuation due to the ML cavity walls, which is much more effective.

Tab. 6 shows that without any specify mitigation for stray fields, the performance loss is within budget. However, natural sources do not pose the greatest risk for performance loss to CLIC. As described in [7], stray fields from natural sources typically have very low frequencies (less than 1 Hz) that are effectively mitigated with a beam-based feedback. Natural sources with frequencies greater than 1 Hz are typically within the 1 nT tolerance

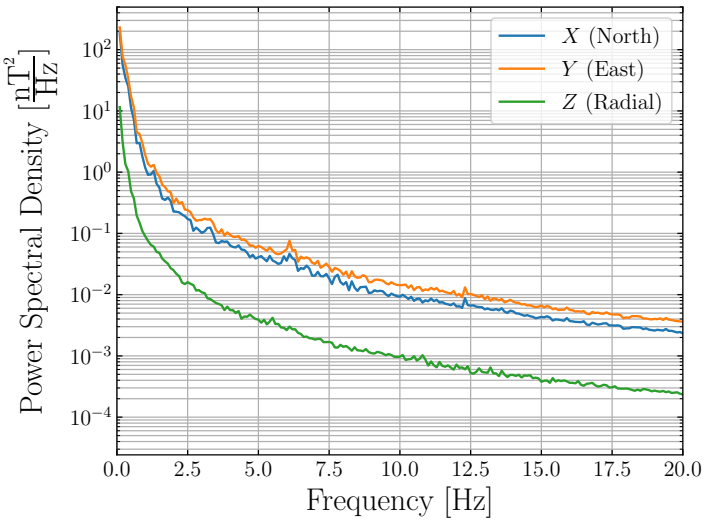

Figure 5: Power spectral density of a geomagnetic disturbance measured in Tihany, Hungary.

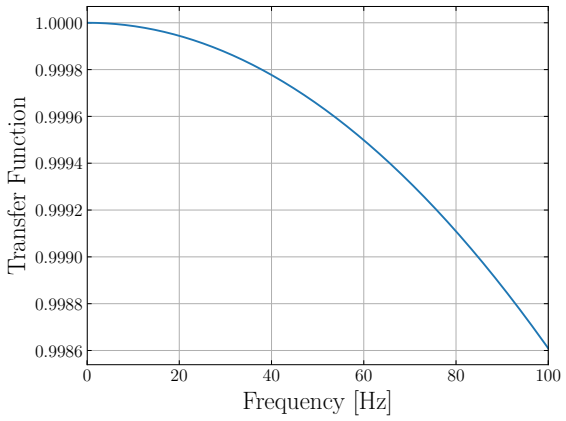

(a) Beam pipe modelled as a cylinder of inner radius 1cm, consisting of 20 μm of copper and 1 mm of steel.

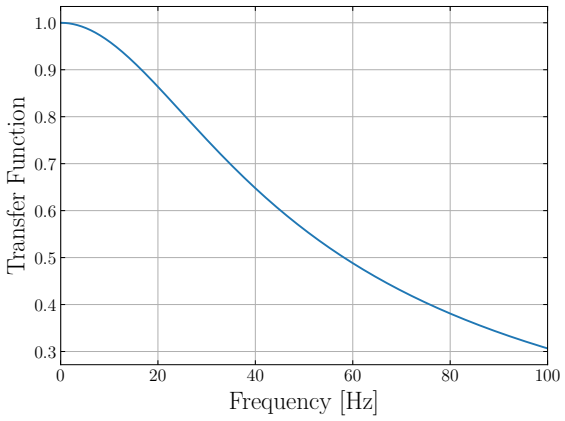

(b) ML cavity walls modelled as a 1 cm cylinder of copper with inner radius 1 cm.

Figure 6: Transfer functions the materials surrounding different sections of CLIC.

for coherent stray fields.

Sources of stray fields that requires more attention are the accelerator elements, such as magnets and RF systems, that constitute CLIC, referred to as technical sources. These are capable of producing stray fields in a wide range of frequencies including the range 1-20 Hz where the beam-based feedback is ineffective and in fact amplifies perturbation to the beam. A mitigation strategy under consideration for dealing with these frequencies is wrapping sections of the beam pipe with a material of high magnetic permeability, such as mu-metal, to act as a magnetic shield that prevents the stray field from reaching the beam. The transfer function of a 1 mm mu-metal coating is shown in Fig. 7.

To characterised the expected magnetic field in an accelerator environment, the background magnetic field in the LHC tunnel and ALICE detector cavern, shown in Fig. 8, was measured. Although this measurement doesn't replicate the exact magnetic environment of CLIC, it does represent the magnetic field that can be expected underground and in the presence of technical equipment. The measurement was taken at a time when the vacuum

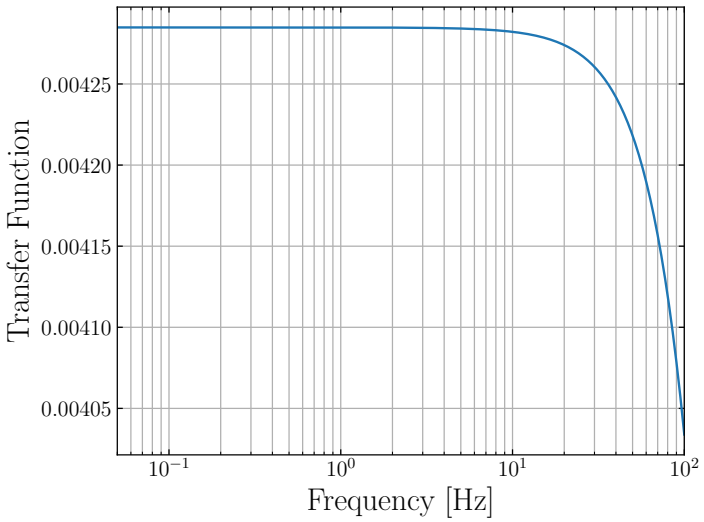

Figure 7: Transfer function of a 1 mm mu-metal coating of inner radius 1 cm. The relative magnetic permeability of the mu-metal used is 10,000.

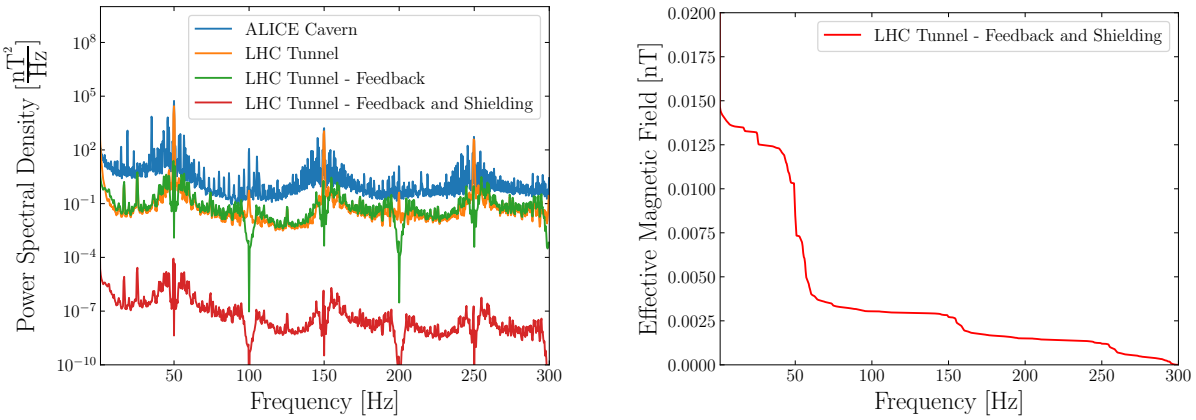

Figure 8: On the left is the power spectral density of the background magnetic field measured near Point 2 of the LHC tunnel and in the ALICE detector cavern measurement on the 31/01/18 along with the effect of different mitigation techniques. On the right is the square root of the integral of the power spectral density.

systems were in operation, however the magnets were not. There is a significantly larger magnetic field in the ALICE detector cavern, highlighting that the detector can act as a technical source. Here, it is clear that the background magnetic field in the LHC tunnel is well above the 1 nT tolerance for coherent stray fields. However, including the effect of a 1 mm mu-metal coating and the beam-based feedback, the magnetic field can be brought to the level of the tightest tolerance of 0.1 nT reported in [6].

The exact design of the mitigation is still to be optimised and will be based upon the on-going measurement campaign to characterise a realistic power spectrum of magnetic fields for CLIC. However, it is expected that a combination of beam-based feedback and magnetic shielding will be able to effectively mitigate the effects of stray fields.

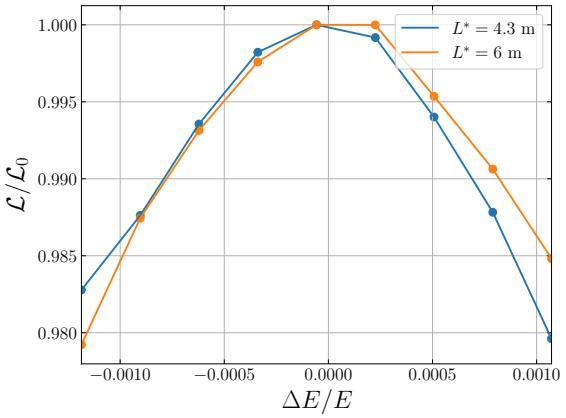

Figure 9: Energy acceptance of two BDS designs.

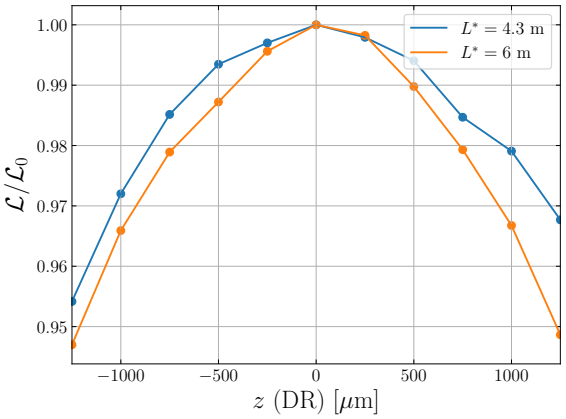

Figure 10: Luminosity against the longitudinal bunch position from the DRs.

5 Longitudinal Stability

An error in the longitudinal bunch position (phase error) can lead to luminosity loss in two ways. The first is the direct impact of the arrival time of the colliding bunches at the IP. If two bunches do not arrive at the same time, they will collide either before or after the nominal collision point, where the beta functions and therefore beam sizes are larger, leading to a luminosity reduction. The second effect is a change of the effective gradient in the ML due to the bunch arriving before or after the nominal phase. This leads to an energy error, which reduces luminosity because of the limited energy acceptance of the BDS.

To investigate the energy acceptance of the BDS, the effective gradient of the ML was varied directly. The energy acceptance of the two BDS designs considered is shown in Fig. 9. Each data point was simulated 100 times with different beam seeds and the luminosity was averaged[1]. The luminosity was calculated with a beam tracked through a lattice with an altered effective gradient in the ML and a reference beam, which was tracked through the ideal lattice with the nominal ML gradient. Therefore, tolerances will be calculated with half the total luminosity loss budget. The energy acceptance of both BDS designs is roughly the same. To remain within a 1 % luminosity loss, the beam energy entering the BDS must be within $\Delta E/E \approx \pm 10^{-3}$. The corresponding effective gradient error that can be tolerated is the same $\Delta G_{\text{eff}}/G_{\text{eff}} \approx \pm 10^{-3}$.

To obtain a phase stability tolerance, a phase error from the DRs was introduced and tracked to the IP. Here, both an error in the effective gradient and arrival time occur, whereas varying the effective gradient does not effect the arrival time of the colliding bunches. Luminosity against the longitudinal bunch position from the DRs is shown in Fig. 10. Each data point was simulated 100 times and the luminosity was averaged. Again, the luminosity was calculated with a reference beam tracked through the ideal lattice, so tolerances are calculated with half the luminosity loss budget.

There is a large phase errror of ± 750 μm that can be tolerated to remain within a 1 % luminosity loss budget. The $L^* = 4.3$ m lattice can tolerate a slightly larger error, however the tolerances are similar for the two BDS designs. The reason why such a large

[1]The reference energy (TCL variable \$e0) used in PLACET simulations to define the BDS lattice was altered from 190.0 to 190.1 for the $L^* = 4.3$ m BDS and to 190.9 for the $L^* = 6$ m BDS in all simulations of longitudinal stability.

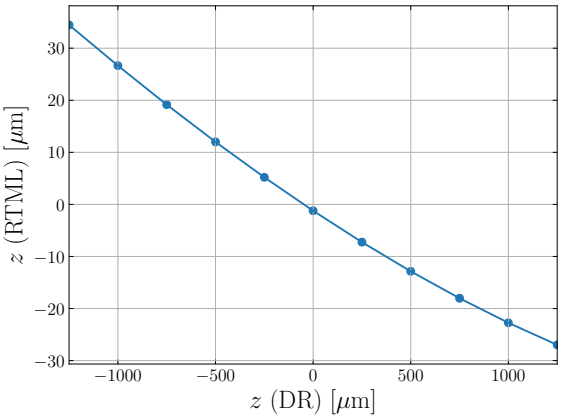

Figure 11: Longitudinal bunch position exiting the RTML against entering the RTML.

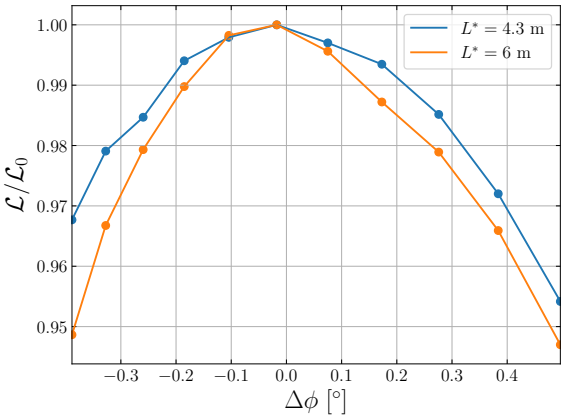

Figure 12: Luminosity against a phase error at the start of the ML. The phase is expressed using the RF frequency of the ML cavities (12 GHz).

phase error from the DRs can be tolerated is due to the bunch is compression that occurs the RTML. The bunch length is compressed by a factor of 26, which leads to a reduction by roughly the same factor in the phase error. A plot of the longitudinal bunch position at the end of the RTML against the start of the RTML is shown in Fig. 11.

Fig. 12 shows the phase error that can be tolerated at the start of the ML. Here, the phase error ($\Delta\phi$) is expressed in terms of the RF frequency in the ML cavities (12 GHz). The ML has a tolerance of $\pm 0.2°$ to remain within a 1 % luminosity loss budget. This is roughly the same for both BDS designs.

References

[1] A. Latina, *et al.*, "Recent Improvements of the Tracking Code PLACET", EPAC'08, Genoa, Italy, June 2008.

[2] D. Schulte, "Beam-Beam Simulations with GUINEA-PIG", ICAP'98, Monterey, CA, USA, Sept. 1998.

[3] J. Snuverink *et al.*, "Impact of Dynamic Magnetic Fields on the CLIC Main Beam", IPAC'10, Kyoto, Japan, May 2010.

[4] E. Marin, D. Schulte, B. Heilig, and J. Pfingstner, "Impact of Dynamical Stray Fields on CLIC", IPAC'17, Copenhagen, Denmark, May 2017.

[5] C. Gohil, P.N. Burrows, E. Marin, D. Schulte, and M. Buzio, "Measurements and Impact of stray fields on the 380 GeV Design of CLIC", IPAC'18, Copenhagen, Denmark, May 2017.

[6] C. Gohil, D. Schulte, and P.N. Burrows, "Sinusoidal Stray Magnetic Field Tolerances for the 380 GeV CLIC Design", CERN, Geneva, Tech. Rep. CERN-ACC-2018-XXXX. CLIC-Note-XXXX, Nov. 2018.

[7] B. Heilig, C. Beggan, and J. Lichtenberger, "Natural sources of geomagnetic field variations", CERN, Geneva, Tech. Rep. CERN-ACC-2018-0033. CLIC-Note-1083, Oct. 2018.